

Quantum-enhanced Markov Chain Monte Carlo for Combinatorial Optimization

Kate V. Marshall,^{1,*} Daniel J. Egger,² Michael Garn,³ Francesca Schiavello,^{3,4} Sebastian Brandhofer,⁵ Christa Zoufal,² and Stefan Woerner²

¹*IBM Quantum, IBM Research Europe – Hursley, United Kingdom.*

²*IBM Quantum, IBM Research Europe – Zurich, Switzerland*

³*The Hartree Centre, STFC, Sci-Tech Daresbury, United Kingdom*

⁴*The Open Quantum Institute, Geneva, Switzerland*

⁵*IBM Quantum, IBM Research Europe – Böblingen, Germany*

(Dated: February 9, 2026)

Quantum computing offers an alternative paradigm for addressing combinatorial optimization problems compared to classical computing. Despite recent hardware improvements, the execution of empirical quantum optimization experiments at scales known to be hard for state-of-the-art classical solvers is not yet in reach. In this work, we offer a different way to approach combinatorial optimization with near-term quantum computing. Motivated by the promising results observed in using quantum-enhanced Markov chain Monte Carlo (QeMCMC) for approximating complicated probability distributions, we combine ideas of sampling from the device with QeMCMC together with warm-starting and parallel tempering, in the context of combinatorial optimization. We demonstrate empirically that our algorithm recovers the global optima for instances of the Maximum Independent Set problem (MIS) up to 117 decision variables using 117 qubits on IBM quantum hardware. We show early evidence of a scaling advantage of our algorithm compared to similar classical methods for the chosen instances of MIS. MIS is practically relevant across domains like financial services and molecular biology, and, in some cases, already difficult to solve to optimality classically with only a few hundred decision variables.

I. INTRODUCTION

Combinatorial optimization is an important application for quantum computing, inspired by the natural formulation of such problems to finding the ground state of Ising Hamiltonians [1]. This mapping has motivated the exploration of quantum optimization algorithms that could offer super-polynomial speedups over classical approaches [2–7]. There exist various approaches to the study of quantum optimization, ranging from provably exact to heuristic algorithms. Heuristic approaches usually lack provable convergence guarantees, runtime guarantees, or both [1]. Nevertheless, these algorithms could outperform classical solvers for select problem instances. In the field of classical optimization, most practically used optimization algorithms are heuristic. One such quantum heuristic is the Quantum Approximate Optimization Algorithm (QAOA) [8], which benefits from bounded worst-case performance guarantees, e.g., for MAXCUT on 3-regular graphs [9]. However, the search for evidence of a quantum advantage has proved extremely challenging, largely due to noise that continues to limit the width and depth of circuits executable on available hardware.

Whilst we navigate these challenges, heuristic quantum-classical frameworks offer a practically motivated direction for near-term quantum computing research [10, 11].

For quantum optimization, methods such as warm-starting leave much to be hopeful about, even before fault-tolerance [1, 11]. Today’s quantum devices—despite inherent noise—have achieved a scale, speed, and fidelity that enable computations beyond the reach of exact classical simulation [12]. Hence, it is now possible to benchmark the capabilities of quantum-enhanced solvers on non-trivial optimization problem instances, such as the ones provided in the Quantum Optimization Benchmarking Library (QOBLIB) [13]. This resource provides a framework consisting of combinatorial optimization problems, benchmarking metrics, and baseline results to assist the community in exploring the path to quantum advantage in optimization. This also enables us to better understand the potential practical usefulness of quantum optimization algorithms in addressing problems that map to industry-relevant applications.

As quantum hardware becomes increasingly capable, we can begin to investigate theoretical results with non-trivial problem instances. One set of interesting theoretical and early numerical results include those from the quantum-enhanced Markov chain Monte Carlo (QeMCMC) algorithm, originally developed for approximating challenging probability distributions [14, 15]. The authors in Ref. [15] showed that with a quantum proposal distribution, QeMCMC demonstrated up to a quartic advantage in reaching the target distribution more efficiently compared to classical Markov chain Monte Carlo (MCMC). Subsequent work has further investigated behavior, limitations, and variants of QeMCMC [16–20].

* kate_marshall@ibm.com

While asymptotic speedups for quantum optimization algorithms are only expected with fault-tolerant quantum devices [21], heuristic quantum optimization algorithms may demonstrate promising results in the near-term for select problem instances. In this work, we introduce and explore an optimization workflow that combines concepts from QeMCMC, warm-starting, and parallel tempering to solve combinatorial optimization problems. We show the first realization of a practical QeMCMC algorithm on non-trivial system sizes. Using our method, we approach instances of Maximum Independent Sets (MIS) of increasing size up to 117 decision variables using IBM Quantum superconducting hardware. Particular instances of this problem class are already challenging to solve with state-of-the-art classical solvers with only a few hundred variables, in some cases [13]. Interestingly, we observe an empirical scaling advantage of our method in terms of increasing problem size, compared to classical MCMC implementations on the selected MIS instances, for the three problem instances studied. Furthermore, for the largest problem instance with 117 decision variables, we observe the quantum hardware experiments converging faster in terms of number of iterations compared to classical simulations of the algorithm, which suggests the truncation error associated with the tensor network simulations becomes more detrimental than hardware noise in our simulations. Hence, our algorithm provides an alternative way to approach combinatorial optimization with quantum computing.

We structure this work as follows. In Section II, we provide background material before presenting key methods used herein in Section III, including QeMCMC, warm-starting quantum optimization and parallel tempering. We explain how these methods work together to form the basis of our workflow in Section III F, accompanied by Figure 1. In Section IV B, we test the applicability of applying the QeMCMC-inspired optimization algorithm to MIS. We provide comparisons to known classical methods in Section IV C, discuss anticipated scaling, or feasibility with increasing problem size, of our algorithm in Section IV D and conclude in Section V.

II. BACKGROUND

A. Markov chain Monte Carlo methods for sampling Boltzmann distributions

Consider a discrete optimization problem defined by an energy or cost function $E(s)$ for configurations $s \in \{-1, +1\}^n$, where the objective is to minimize this energy. Once an energy function is defined, we may associate to it the Gibbs distribution, or equivalently the Boltzmann distribution of a classical Ising model,

$$\mu(s) = \frac{e^{-E(s)/(k_B T)}}{Z}, \quad (1)$$

where $Z = \sum_s e^{-E(s)/(k_B T)}$ is the partition function ensuring normalization, and k_B is the Boltzmann constant. At low temperatures, i.e., $T \rightarrow 0$, the distribution in Eq. (1) concentrates its probability mass on configurations that minimize $E(s)$, which provides a connection between probabilistic sampling and optimization. Constraints may be incorporated into the energy landscape, e.g., by adding penalty terms of the form

$$E(s) = E_0(s) + \lambda C(s), \quad (2)$$

where $E_0(s)$ denotes the objective, $C(s)$ tracks constraint violations, and λ is a sufficiently large penalty factor, or Lagrange multiplier. In the limit $T \rightarrow 0$, the Gibbs distribution concentrates probability mass on low-energy configurations, biasing sampling toward high-quality solutions.

In general, constructing a low-temperature Gibbs state from which to sample is computationally hard. Therefore, in practice, MCMC methods are widely used to sample from Boltzmann distributions [22]. MCMC avoids explicitly evaluating the target distribution μ and its associated partition function, Z , since this requires summing over an exponentially large configuration space, and thus, exact computation would require $\Omega(2^n)$ time. Instead, MCMC constructs a Markov chain that evolves through the space of spin configurations by proposing transitions from a current configuration s to a candidate configuration s' , according to a fixed transition probability, $P(s' | s)$. A common approach is a two-step proposal and acceptance procedure

$$P(s' | s) = Q(s' | s) A(s' | s). \quad (3)$$

Here, $Q(s' | s)$ denotes the conditional probability of proposing candidate transitions from s to s' , and $A(s' | s)$ is an acceptance ratio. A can be defined in numerous ways, with a popular example being the *Metropolis Hastings (MH)* acceptance probability

$$A(s' | s) = \min\left(1, \frac{\mu(s') Q(s | s')}{\mu(s) Q(s' | s)}\right). \quad (4)$$

To ensure this procedure yields meaningful samples, the transition probabilities P must be designed such that the chain converges to our target distribution, μ , from Eq. (1). This convergence is guaranteed under standard conditions—namely irreducibility and aperiodicity—and by enforcing the detailed balance condition,

$$P(s' | s) \mu(s) = P(s | s') \mu(s'), \quad (5)$$

for all $s \neq s'$ [15]. This detailed balance constrains P such that the Markov chain converges to μ as its stationary distribution. In this regime, samples are statistically correct, meaning that they are drawn from the target, μ , and computed averages converge to the true expectation values without systematic bias [15].

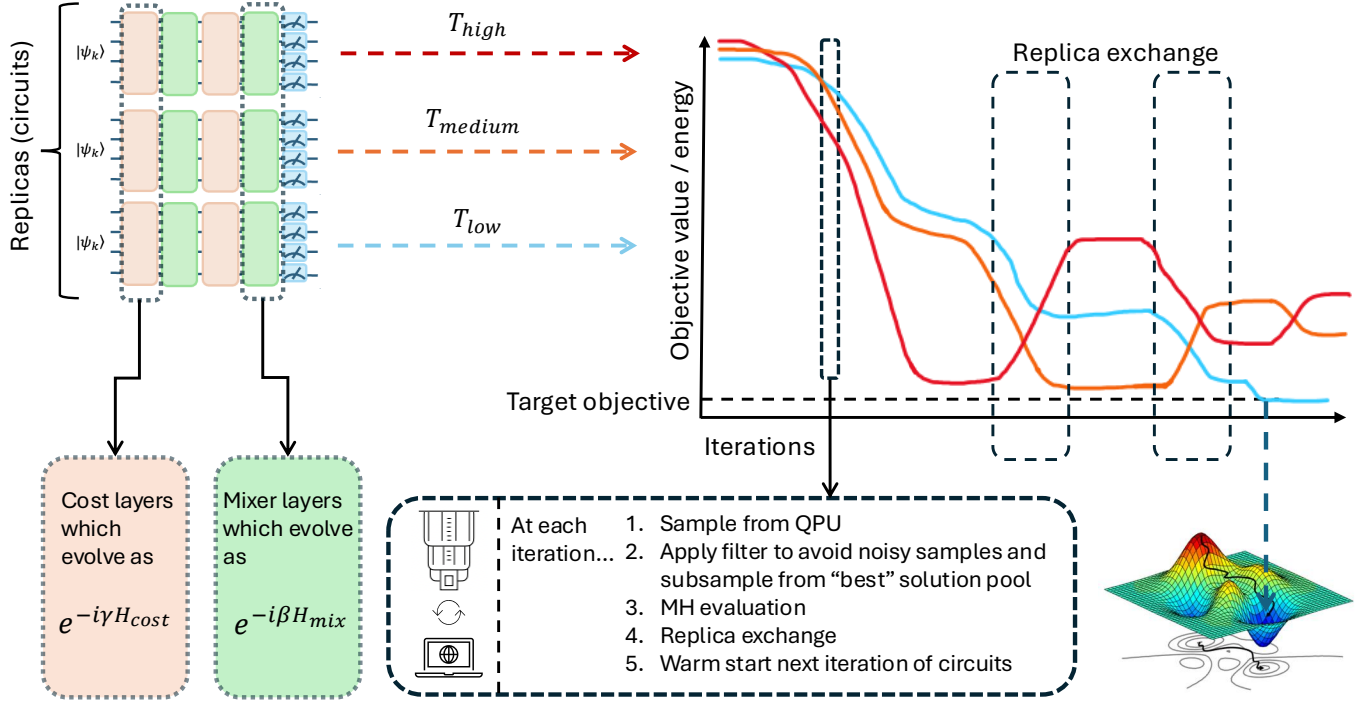


FIG. 1: The algorithm workflow. We see a hot, medium and cold replica working together such that the coldest replica eventually converges to the target objective. Objective values of proposed solutions to the MIS problem are plotted against iterations. Each iteration requires drawing samples from the QPU and then classically processing these counts, necessitating a close exchange of information between quantum and classical hardware.

In the worst case, computation time required to obtain independent samples for the MH variant of MCMC, described above, scales exponentially with system size. Yet, in practice, it is often possible to choose good proposal distributions that exhibit good convergence. This forms the basis of widely-used classical optimization heuristics such as simulated annealing and parallel tempering [23–25]. An end-to-end example of sampling from the Boltzmann distribution with our implementation of QeMCMC is provided in Appendix A.

B. Maximum Independent Sets

In this manuscript, we study MIS problems, which we will now formulate as a Quadratic Unconstrained Binary Optimization (QUBO) problem that can be mapped to a classical Ising model. This mapping enables us to interpret the problem in terms of an energy landscape and to sample from the corresponding Boltzmann distribution, where low-temperature sampling concentrates on configurations with a minimized energy.

Let $G = (V, E)$ be a graph with vertices $V = \{v_1, \dots, v_n\}$ and edges $E \subset V \times V$. An independent set of vertices of G is a subset of V such that no pair of vertices in the subset

is connected via an edge in E . A maximum independent set is an independent set of maximal size. Now, suppose a binary decision variable $x_i \in \{0, 1\}$ for each vertex v_i , where $x_i = 1$ if v_i is included in the selected subset of vertices, and $x_i = 0$ otherwise. Then, the MIS problem can be formulated as

$$\max_x \sum_{i=0}^{|V|-1} x_i, \quad (6)$$

subject to the constraints

$$x_i x_j = 0 \quad \forall (v_i, v_j) \in E, \quad (7)$$

which enforce the selected subset of vertices to be an independent set. Further, we can formulate this as the following QUBO:

$$\max_x \left(\sum_{v_i \in V} x_i - \lambda \sum_{(v_i, v_j) \in E} x_i x_j \right), \quad (8)$$

where the first term is the objective and the second term enforces the constraints as long as λ is sufficiently large, e.g., $\lambda \geq 2$, i.e., the maximum in Eq. (8), indeed gives an optimal MIS solution.

We convert this QUBO to the Hamiltonian

$$H_{\text{cost}} = H_{\text{objective}} + \lambda H_{\text{constraint}}, \quad (9)$$

where $H_{\text{objective}}$ and $H_{\text{constraint}}$ are derived and explained using the standard mapping in Appendix B.

In this form, each spin configuration corresponds to a candidate solution and has an associated energy $E(s)$, obtained by evaluating the Ising Hamiltonian on that configuration. This energy function defines the Ising model and induces a Boltzmann distribution over configurations, as introduced previously in Eq. (1). Sampling from this distribution at temperatures, T , allows exploration of the solution space.

In the limit as $T \rightarrow 0$, the distribution concentrates on configurations that minimize $E(s)$, which corresponds to optimal solutions of MIS. Here, we choose values of the Lagrange multiplier, λ , that do not directly enforce a feasible subspace of configurations, but instead penalize solutions with constraint violations. The choice of this term involves balancing the objective and constraints of our problem, trading feasibility with cost of solutions. The process used to optimize for both objective and constraints is described in Appendix C.

III. METHODS

A. Quantum-enhanced Markov chain Monte Carlo

In Ref. [15], the authors propose a quantum-enhanced MCMC scheme in which a quantum circuit is used to generate the proposal distribution. This work was motivated by the fact that classical MCMC approaches struggle to explore rugged energy landscapes at low T , which are typical when studying spin glass behavior. The quantum-enhanced MCMC algorithm generates proposed configurations by sampling from a quantum circuit, drawn from a discretized annealing Hamiltonian [15]:

$$H = (1 - \kappa) \alpha H_{\text{cost}} + \kappa H_{\text{mix}}. \quad (10)$$

There is evidence that this sampling procedure can accelerate MCMC convergence in spin glasses at low T with up to a quartic speedup. Here, H_{cost} encodes the classical model, H_{mix} is a mixing Hamiltonian, $\kappa \in [0, 1]$ controls the relative weights of both operator terms and α is a normalization factor that rescales the objective term such that its magnitude is comparable to that of the mixer Hamiltonian. More details are found in Ref. [15]. We can view the penalized energy function introduced in Eq. (2) as the classical counterpart of this Hamiltonian.

It is then possible to obtain a new configuration s' by preparing the computational basis state $|s\rangle$ on the quantum device, and applying unitary U , given by

$$U(t) = e^{-iH(\kappa)t}. \quad (11)$$

We then measure the state $U|s\rangle$ to sample the configuration proposal s' . Crucially, a key insight made by the authors in Ref. [15] included that we can avoid explicitly computing the ratio of transition probabilities, Q , making the computation of A in Eq. (4) tractable. This finding enabled much of the authors' novel experiments and results. This is achieved by constructing circuits from Eq. (10), where U satisfies the symmetry constraint

$$|\langle s'|U|s\rangle| = |\langle s|U|s'\rangle|. \quad (12)$$

The ratio of distributions in Eq. (4) then cancels out by setting $Q(s' | s) = Q(s | s')$ for all configurations $s, s' \in \{-1, 1\}^n$. The symmetry condition in Eq. (12) ensures reversibility of transitions between configurations, or detailed balance, which is required to guarantee convergence to the target distribution, μ , as defined in Eq. (1). Each qubit is measured in the computational basis, denoting the outcome s' , before choosing whether to accept or reject the proposed configuration using the acceptance probability defined in Eq. (4). If s' is rejected, the chain remains at the current state s .

B. Warm-starting QAOA

Using a first-order Trotter decomposition of the Hamiltonian in Eq. (10), the evolution operator U defined in Eq. (11) can be constructed much like QAOA. Thus, when we apply the unitary to the basis state $|s\rangle$, like $U|s\rangle$, this resembles warm-starting QAOA, which we now review.

Warm-starting QAOA has proved a popular technique in the recent quantum optimization literature [26–33]. The original idea comes from leveraging good solutions determined by a (usually classical) algorithm to initialize another (usually quantum) algorithm, to further improve the results. In Ref. [26], the authors initialize a QAOA circuit from bitstring $s \in \{0, 1\}^n$, either obtained classically, or in our case, from a previously accepted quantum sample. Since the QAOA cost operator has no impact on a state made of a single computational basis state, the authors introduce a regularization parameter ε , which instead prepares a superposition of states in a neighborhood of s . We control the spread of the quantum state around s by setting $\varepsilon \in (0, 1/2)$ and defining a softened version of s , where for each bit i of configuration s , we define

$$\tilde{s}_i = \begin{cases} \varepsilon, & s_i = 0, \\ 1 - \varepsilon, & s_i = 1. \end{cases}$$

The softened solution \tilde{s} is then used to define single-qubit rotation angles,

$$\theta_i = 2 \arcsin(\sqrt{\tilde{s}_i}),$$

producing the state

$$|\psi(\theta)\rangle = \bigotimes_{i=1}^n R_y(\theta_i) |0\rangle = \bigotimes_{i=1}^n \left(\cos \frac{\theta_i}{2} |0\rangle + \sin \frac{\theta_i}{2} |1\rangle \right), \quad (13)$$

or, equivalently,

$$|\psi(\tilde{s})\rangle = \bigotimes_{i=1}^n \left(\sqrt{1 - \tilde{s}_i} |0\rangle + \sqrt{\tilde{s}_i} |1\rangle \right). \quad (14)$$

The same θ_i -dependent R_y rotations are used in both the warm-started initial state and the associated mixer. The mixer is adjusted such that its ground state is $|\psi(\tilde{s})\rangle$. This results in solutions to MIS with a bias towards some known good starting point [26].

C. Parallel tempering

When sampling from the Boltzmann distribution of Ising models at low temperatures, the energy landscape typically becomes rugged, characterized by numerous local minima separated by high energy barriers. At low temperatures, classical MCMC methods generally suffer from slow convergence because of long mixing times, i.e., the number of steps a Markov chain must run before its distribution is close enough to the stationary distribution such that samples can be considered representative. In addition, classical MCMC methods may become trapped in local energy minima at low temperatures. To mitigate this behavior, parallel tempering or replica exchange is employed in MCMC procedures [34–36]. This approach introduces multiple replicas of the system, each at a different temperature, where the high-temperature replicas explore the energy landscape aggressively, while low-temperature replicas ensure accurate sampling of the target distribution, by closely tracking local minima. Parallel tempering is described in more detail in Refs. [37, 38].

To begin, we consider N replicas of the same system, where each replica $i \in \{1, \dots, N\}$ represents the same Ising model but at a different temperature T_i . Temperatures are typically ordered $T_1 < T_2 < \dots < T_N$. Each replica i evolves independently using its own Markov chain, targeting the Boltzmann distribution, μ , defined in Eq. (1). A single iteration of the parallel tempering algorithm then consists of two steps:

1. *Local MCMC updates:* Each replica i performs a number of standard MCMC updates at its own temperature.
2. *Replica exchange stage:* Exchange proposed configurations between selected pairs of replicas i and j (for more details, see Appendix D), which can help low energy replicas escape local minima, with

probability

$$A_{\text{exchange}}(s_i, s_j) = \min \left(1, \exp \left[\left(\frac{1}{T_i} - \frac{1}{T_j} \right) (E(s_j) - E(s_i)) \right] \right). \quad (15)$$

This allows a high temperature Markov chain to discover a “good” candidate solution and transfer it to a low temperature chain, or replica, which will accurately sample around it. These two steps are repeated until the stopping criterion has been satisfied, i.e., we converge to the target objective.

D. Mitigating noisy samples

For sampling experiments running on noisy quantum computers, there are fewer known techniques for mitigating the impact of noise than for computing expectation values, see Refs. [39–42]. Recently, the authors of Ref. [43] propose to increase the number of samples by $1/\sqrt{v}$, where v measures the noise strength in the circuit, and prove bounds on noise free expectation values [43, 44]. The noise strength v can be measured explicitly or estimated using gate errors provided, e.g., by the IBM Quantum Platform API following compilation of the circuit [45]. By taking $1/\sqrt{v}$ number of samples, the theory explains that we expect at least one sample from the noise-free distribution corresponding to the target quantum circuit, i.e., in an optimization setting, the additional shots guarantee that we have at least the same performance as in the corresponding noise-free experiment. Where possible, we take the total number of shots or samples suggested via this method in our experiments. Where the requested number of samples is unfeasible, such as when circuits are very deep, we choose to use 10,000 shots, such that the runtime remains practical. This makes sense for an optimization setting, since not all errors affect the final solution, and noise can help to move closer to the target objective in some cases. Thus, using fewer shots than this theoretical quoted bound can still be successful.

We evaluate and rank the objective values of all samples and choose to keep the lowest-energy, i.e., the best, samples. This introduces a bias towards good solutions, which is desirable in the context of our optimization task. We test both taking the best single low-energy sample from the distribution of results, as well as subsampling from a portion of, say 10, of the lowest-energy bitstrings, to maintain some balance of exploration of the cost landscape, i.e., escaping local minima, and exploitation of good solutions. Duplicate solutions at the cutoff point are retained, such that we still favor resampled solutions from the circuit.

Parameter	Symbol	Optimization method
Cost Hamiltonian evolution angle (QAOA)	γ	Classical optimization pipeline [46]
Mixer Hamiltonian evolution angle (QAOA)	β	Classical optimization pipeline [46]
MIS constraint term (Lagrange multiplier)	λ	Classical optimization pipeline [47]
Regularization parameter for warm-starting	ε	Experimentally informed, see Appendix C
Temperature range used for parallel tempering setup	$[T_{\text{low}}, T_{\text{high}}]$	Determined via formulae, see Appendix D
Number of replicas used for parallel tempering setup	N_{replicas}	Design choice, see Appendix D
Replica exchange regularity	Δt_{swap}	Experimentally informed, see Appendix D

TABLE I: Summary of parameters, their roles and optimization method for each problem instance.

E. Circuit construction

We construct circuits from Eq. (10) that resemble QAOA, using a first-order Trotter decomposition, since Trotter error is not relevant. Since $[H_{\text{cost}}, H_{\text{mix}}] \neq 0$, Eq. (10) cannot be implemented exactly as a single exponential. The Lie-Trotter decomposition,

$$e^{-itH} \approx e^{-it(1-\kappa)\alpha H_{\text{cost}}} e^{-it\kappa H_{\text{mix}}} + \mathcal{O}(t^2), \quad (16)$$

divided into two identical Trotter steps yields

$$e^{-itH} \approx (e^{-i\gamma H_{\text{cost}}} e^{-i\beta H_{\text{mix}}})^2, \quad (17)$$

with fixed angles

$$\gamma = \frac{t}{2}(1-\kappa)\alpha, \quad \beta = \frac{t}{2}\kappa. \quad (18)$$

This construction has the form of a $p = 2$ QAOA circuit with parameters, $\gamma_1 = \gamma_2 \equiv \gamma$ and $\beta_1 = \beta_2 \equiv \beta$. Details on how γ and β parameters are trained are found in Appendix C. Our unitary in Eq. (11) has the form

$$U_{\text{QAOA}} = e^{-i\beta_2 H_{\text{mix}}} e^{-i\gamma_2 H_{\text{cost}}} e^{-i\beta_1 H_{\text{mix}}} e^{-i\gamma_1 H_{\text{cost}}}. \quad (19)$$

Throughout this work, we use a warm-started variant of the standard transverse-field mixer, $H_{\text{mix}} = \sum_{i=1}^n X_i$. H_{cost} is defined in Eq. (9).

Since our circuits structurally resemble QAOA, in order to run QeMCMC-like experiments, we cannot simply initialize U_{QAOA} in the computational basis state $|s\rangle$, as per Ref. [15]. When using this initialization with the form of the standard transverse-field mixer, we see no exploration of the solution space, as noted in Ref. [29]. Instead, we adapt the warm-starting QAOA procedure from Section III B, restricting the sample space used for our quantum proposal distribution, Q , to the best, low-energy portion. This, in combination with the bias introduced from Section III D, distinguishes us from the original goals of QeMCMC, developed in the context of sampling from Boltzmann distributions. Instead, we seek the ground state of an Ising Hamiltonian framing our optimization problem. We propose candidate updates $s_k \rightarrow s_{k+1}$, according to our proposal distribution $Q(s_{k+1} | s_k)$. This is done by applying the unitary, U_{QAOA} , in Eq. (19) to $|s_k\rangle$, and defining transition probabilities from the resulting measurement statistics.

Crucially, since we introduce these asymmetric proposal distributions in our sampling procedure, the convergence guarantees of QeMCMC originally positioned by the authors in Ref. [15] no longer hold. Our approach is, therefore, purely a heuristic one.

Finally, as MIS problem instance sizes grow, the width and depth of our QAOA ansaetz representing the full graph become too large to run on quantum hardware. Therefore, we construct ansaetz from a simplified cost Hamiltonian obtained by dropping Pauli terms that require too many SWAP gates to implement. For further details, see Appendix E.

F. Experimental Workflow

We combine these methods to build the algorithm visualized in Figure 1 and summarized herein. Firstly, we define a number of identical replica circuits and tune the temperature ladder for these circuits to operate, as described in Section III C and Appendix D. For each circuit, we sample an initial configuration uniformly at random, i.e., $s_0 \sim \mathcal{U}(\{-1, +1\}^n)$, and then proceed as follows:

1. We sample from our parametrized replica circuits derived from Eq. (10). Parameters are classically pre-trained, as described in Appendix C.
2. We take many samples, in order to mitigate the impact of noise on the quantum device, as per the theory described in Section III D. Then, we evaluate the energy $E(s)$ for each sample, filter for a certain number of low energy samples, and randomly subsample one configuration from these.
3. Next, we classically evaluate the proposed solution using the MH criteria defined in Eq. (4).
4. At regular intervals, replicas are allowed to exchange accepted solutions according to the probability defined in Eq. (15), which helps low temperature replicas escape local minima.
5. The accepted solution s_k is used to generate subsequent candidate updates $s_k \rightarrow s_{k+1}$, according to the proposal distribution $Q(s_{k+1} | s_k)$, as described in Section II A. This is done using the warm-start QAOA procedure explained in Section III B.

We repeat this loop for a maximum of 200,000 iterations, or until convergence to the target objective. Our algorithm has many parameters, which we tune using a combination of analytical guidelines drawn from the literature, in addition to heuristic tuning. These parameters differ for each problem instance. A table of the relevant optimizable parameters is presented in Table I. This tuning of parameters strongly influence mixing efficiency and convergence [37, 48–50]. Further details regarding parameter tuning for each MIS problem instance is explored further in Appendices C and D.

IV. RESULTS

We study three different problem instances, most of which are taken from the QOBLIB [13], executed both in simulation and on IBM quantum hardware. These instances are derived from real-world animal social interaction networks, with qubit or node counts $n \in \{17, 52, 117\}$ and corresponding edge counts $m \in \{91, 516, 1027\}$. These graphs share a common provenance and representation as simple, undirected interaction networks. As social networks, they exhibit heterogeneous degree distributions and nontrivial interaction structure, while varying in size and density. Together, these instances provide a natural progression in problem size for probing the scalability of our algorithm. In the remainder of this Section, we focus on the 117 node problem.

A. Simulation results

The algorithm is used to solve MIS problems both using matrix product state (MPS) simulation and on IBM quantum hardware. Simulations were conducted with the *Qiskit Aer* MPS simulator, with a truncation thresholds between of 1×10^{-6} and 1×10^{-10} . This threshold is defined as the number of Schmidt coefficients for which the sum of their squares is smaller than the threshold [51]. Outside of this threshold, values are discarded.

Replica	Temperature	% convergence across 10 repeats	Median convergence
1	0.01	10.0%	863
2	0.11	30.0%	796
3	0.21	20.0%	706
4	0.51	10.0%	619
5	1.01	0%	—

TABLE II: Replica convergence statistics for 5 replicas across 10 independent repeats of simulated experiment for 117 node graph problem instance.

In Table II, we see the number of iterations needed to converge to the target objective (within a maximum of 200,000 iterations). These results are also visualized in Appendix D.

We see that colder replicas have a higher rate of success in converging to their target values, but that a warmer replica, Replica 4, was able to converge in the fewest number of iterations in total, likely due to its more broader search behavior.

B. Hardware results

When running on real quantum hardware, the subsampling procedure used to mitigate against noisy samples for each of these problem instances, is defined in Table III. In Figure 2, we see the global optimum is recovered after 151 iterations on the hardware. 10,000 shots are taken per iteration, followed by randomly subsampling from the best ten samples, using the CVaR method presented in Section III D. For the winning replica, represented in orange, the Hamming distance between accepted solutions at each iteration is displayed.

Experimental results show that the quantum hardware exceeds expectations in terms of algorithm performance indicated from our classical MPS simulations, presented in Table II, since convergence was achieved in fewer iterations on hardware than simulation. This is likely due to truncation error dominating in the noiseless MPS simulation for such a large system, since we observe worsening performance with increased truncation error introduced to the MPS experiments via controlled testing.

A table of all hardware results for the problem instances of 17, 52 and 117 nodes can be found in Table III. We report the maximum number of SWAP layers allowed for the simplified ansaetz for these problems, alongside the associated 2-qubit gate counts and depths. We also provide the estimated upper limit on samples required to compensate the impact of noise, in addition to the number of samples actually taken where this estimated value is unfeasible on hardware, alongside the number of iterations to converge.

C. Baseline comparison studies

The most natural comparison for our heuristic QeMCMC algorithm, is to first understand the capabilities of classical replica exchange MCMC. In this Section, we compare results for the 117 node instance. There exist various possible metrics to compare these experiments, including number of samples, iterations, or wall-clock time. It is usual for standard MCMC to take one sample per iteration, and evaluate this proposal using the MH criteria in Eq. (4). We begin by comparing results in this setting. The top plot in Figure 3 demonstrates our quantum algorithm using 1-shot per iteration with a noiseless MPS simulation. We use classical simulation since the anticipated runtime using quantum hardware was excessive and considered not a sensible use of resources for the 1-shot regime, since each sample is likely not noise-free.

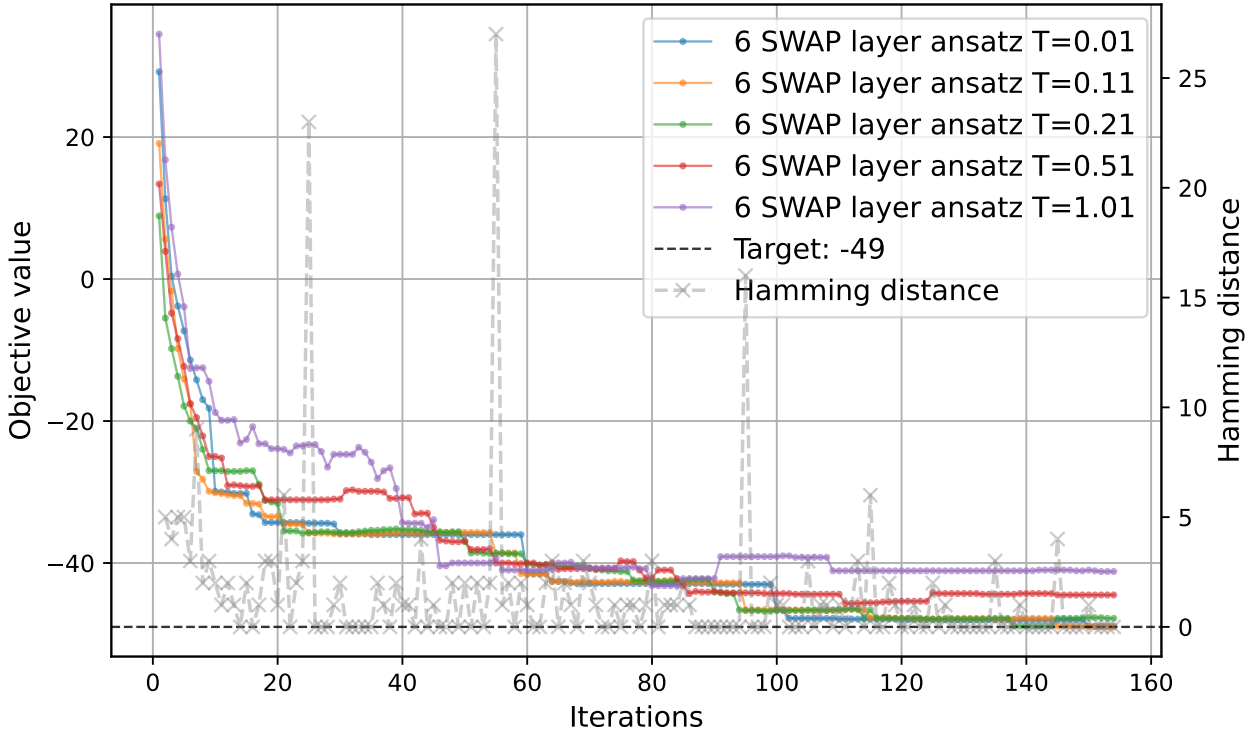


FIG. 2: Parallel tempering experiment run on `ibm_boston` for the 117-node MIS problem. The left axis indicates the progress of objective values per iteration. We see the global optimum is found after 151 iterations, with 10,000 shots per iteration and a random sample taken from a smaller portion of these. The Hamming distance between accepted solutions is also plotted for each iteration for the winning replica in orange, corresponding to the right axis.

Device	Problem instance (nodes)	Max. SWAP layers	2q gate count	2q gate depth	Iterations to converge	Est. shots per iteration	Shots used per iteration	Post-processing comments
ibm_aachen	17	—	740	96	32	5	5	Best sample taken
ibm_aachen	17	—	740	96	2	5	10,000	Sample from best ten
ibm_aachen	52	13	1964	84	81	41×10^9	10,000	Sample from best ten
ibm_boston	52	13	1964	84	17	24,503	10,000	Sample from best ten
ibm_boston	52	37	5532	228	37	4,280,674	100,000	Sample from best ten
ibm_boston	117	6	1574	42	151	30,426	10,000	Sample from best ten
ibm_pittsburgh	117	6	1574	42	114	1,034,484	10,000	Best sample taken

TABLE III: Summary of notable experimental results. All experiments operated with 5 replicas. The estimated number of shots per iteration are derived from the logic explained in Section III D, where differences in how the devices experience noise results in different values for estimated numbers of shots required per iteration. At the time of writing, error rates were lowest for the `ibm_boston` device, followed by `ibm_pittsburgh` and `ibm_aachen`.

In these simulations, experiments converge in a median of $\sim 90,000$ shots across ten trials, where median was the most favorable metric for convergence for both classical and quantum implementations. This is reasonably efficient considering the results presented for the experiment on the `ibm_boston` quantum device in Figure 2 took at least 1.51×10^6 shots (for the winning replica). The performance seen in this top plot of Figure 3 is easily outperformed in $\sim 6,000$ shots required by standard

MCMC, presented in the middle plot of this same Figure 3. Since we are limited from testing this setup on hardware, alternative setups are tested which provide a valid point of comparison, in terms of iterations of the algorithm where each iteration is more costly in number of shots. This setup makes better use of scarce quantum computing resources. An example is seen in Figure 2, where we take 10,000 shots per iteration of the algorithm.

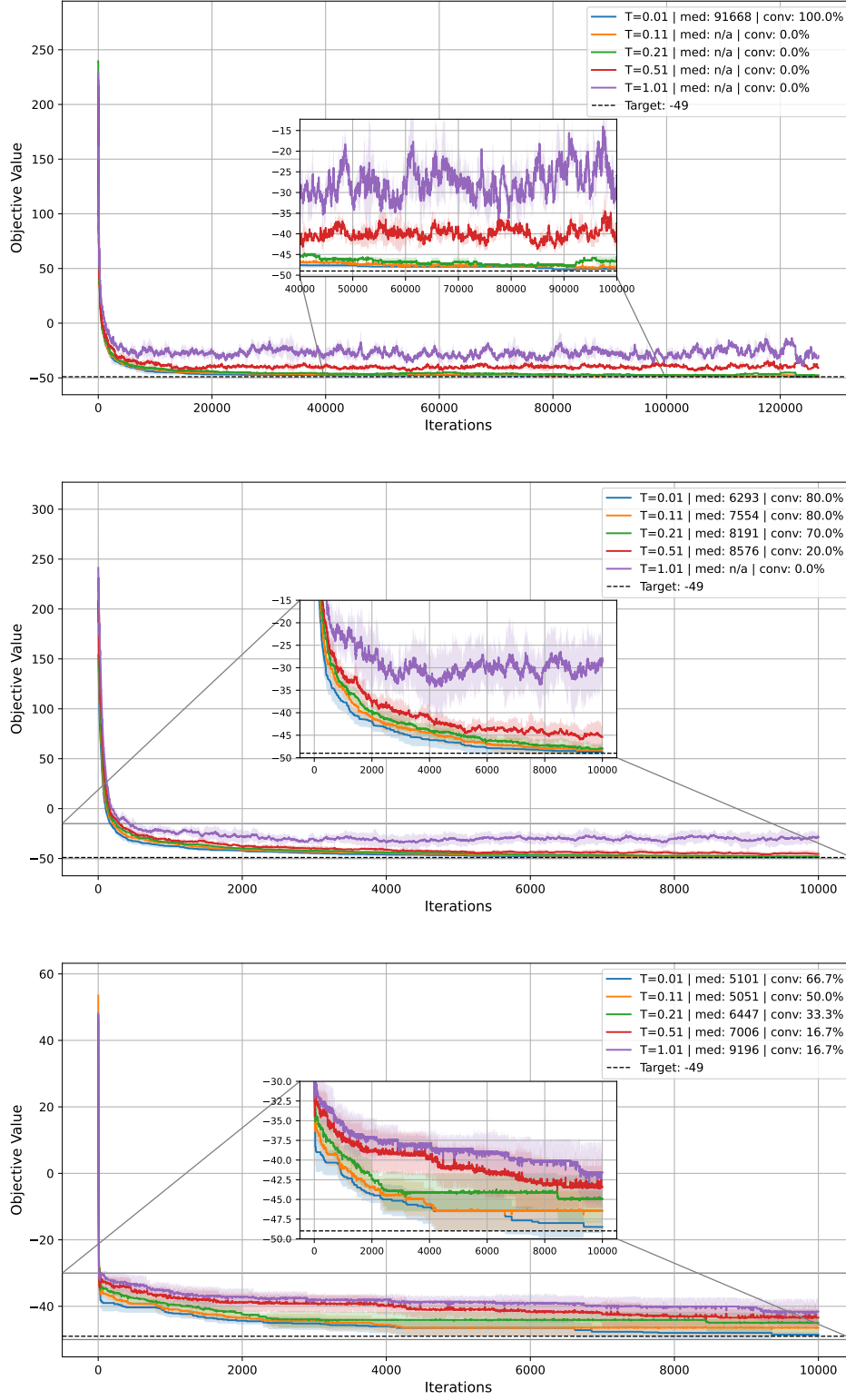


FIG. 3: Comparison of experimental setups for 117 node problem instance experiments. Simulations of the quantum-enhanced algorithm are compared to classical MCMC methods used to find the target objective. In the top plot, we present an MPS simulation of the quantum-enhanced algorithm. Across ten repeats, the target objective is found after a median of $\sim 90,000$ iterations for the coldest replica, with 1-shot per iteration. The middle plot shows a comparison to a classical MCMC simulation, which also uses 1-shot per iteration. Across ten repeats, the target objective is found in $4,000 - 8,000$ iterations for the coldest replica, with a median of $\sim 6,000$ shots, or iterations. Finally, in the bottom plot, we display another classical MCMC simulation, where across ten repeats, the target objective is found in $4,000 - 8,000$ iterations for the coldest replica, with a median of $\sim 5,000$ iterations, in this case using 10,000 shots per iteration and a random sample taken from the best ten proposals.

The number of shots taken per iteration is significantly less than the estimated number of shots required to compensate for noise, reported in Table III. However, since these estimations are upper bounds (see Section III D), in practice, we tune the number of shots such that we can expect a reasonable anticipated runtime on device, usually to 10,000 shots per iteration. From these 10,000 shots, we randomly subsample from the best ten proposals, as described in Section III D and III F. Simulated convergence metrics of this setup are presented in Table II, where convergence is reported in $\sim 600 - 900$ iterations. We observe the results from the quantum hardware require far fewer iterations to converge, see Figure 2, where the experiment converges in 151 iterations compared to the median convergence reported of 796 for the same replica across ten repeats in classical simulation of the quantum experiment. Presumably, this is because truncation error in this regime becomes more detrimental than hardware noise, since it is observed that performance worsens with increased truncation threshold.

For completeness, we also allow this equivalent experimental setup with the classical proposal distribution, using classical MCMC replicas. We take the exact same setup with 10,000 shots per iteration and apply this to the classical case, with random subsampling from the best ten ranked solutions. This result is presented in the bottom plot in Figure 3, where we see convergence is comparable in terms of number of iterations to the classical MCMC results for the 1-shot experimental setup, shown in the middle plot of Figure 3. This gives us confidence that this adapted experimental setup is reasonable. Nevertheless, results from this classical MCMC simulation shown in the middle plot of Figure 3 converge within $4,000 - 8,000$ iterations, with a median of $\sim 5,000$ iterations. This is an order of magnitude larger in terms of number of iterations than the quantum-enhanced algorithm, both in simulation and with regards to results from the real quantum hardware.

Additionally, variations of 1- and 2-distance local searches were tested, which were considered standard baseline comparisons for this type of optimization algorithm. None of these converged within 200,000 allowed iterations. Various combinations of standard MCMC tests were explored, including up to 25 bitflips per sample for each replica, as informed by the Hamming distance between subsequent accepted solutions, s , on the quantum hardware, see Figure 2. The most competitive classical comparison was the classical MCMC setup described above, with up to 5 bitflips allowed per iteration. Finally, we explored alternative quantum-enhanced variants of the algorithm, including an equivalent non-warm started $p = 2$ QAOA approach, which suffered from a finite size effect beyond the 17 node problem instances. We also tested a warm-started $p = 0$ setup, where circuits are composed purely of the (warm-started) initial state only, with no cost or mixer layers. Again, none of these tests were seen to converge to the global optimum.

All comparison studies were initialized from the same starting point, which was drawn from sampling the non-warm started $p = 2$ QAOA circuit. The studied problem instances have been solved to optimality using CPLEX, which provides reference target objectives represented across Figures documented in this paper [52].

D. Scaling analysis

In the previous Section IV C, we discuss the difficulty in comparing classical and quantum-enhanced MCMC approaches within this parallel tempering framework for solving optimization problems. Classical MCMC approaches perform well in a 1-shot per iteration experimental setup, whereas the quantum-enhanced case performs more efficiently if we take many shots per iteration. Therefore, it is useful to look instead at the scaling behavior of both approaches, looking at both number of samples and number of iterations, as we aim to solve larger and more complex problem instances.

To understand whether there is interesting systematic behavior for solving optimization problems of increasing size with both the classical and quantum-enhanced MCMC approaches in this parallel tempering framework, we refer to Figure 4. Although only three related problem instances have been studied, this plot provides a very early indication of how we might anticipate performance scaling for the algorithm presented in this manuscript, with increasing problem instance size as a proxy metric for problem difficulty.

For the classical and simulated quantum-enhanced algorithm, ten independent trials were run and various statistics computed for each of the three problem instances represented in the Figure 4. The median values are plotted for both number of shots and/or iterations as an indication of convergence rate for these implementations. In the first subplot of Figure 4, with the 1-shot experimental setup, we see the classical MCMC algorithm outperforming the simulated quantum-enhanced experiment for each of the three problem instances. As mentioned previously, it was not possible to run this experiment on hardware as the anticipated time required on the quantum device for this 1-shot setup was unfeasible. However, we are primarily interested in the slopes of the fitted lines in Figure 4, which translate to the exponential growth rates. In the left-hand plot of Figure 4, the gradient of the line for the MPS simulation of the quantum algorithm grows at $\sim 86\%$ of the classical rate, suggesting early evidence of a scaling advantage of the quantum-enhanced algorithm, at least for the three studied problem instances. In the right-hand subplot of Figure 4, 10,000 shots are taken from each iteration. We randomly subsample from the best solutions to compensate for noise, as described in Section III D. We see that the fitted line for the classical non-standard MCMC implementation is more performant only with the smaller problem sizes.

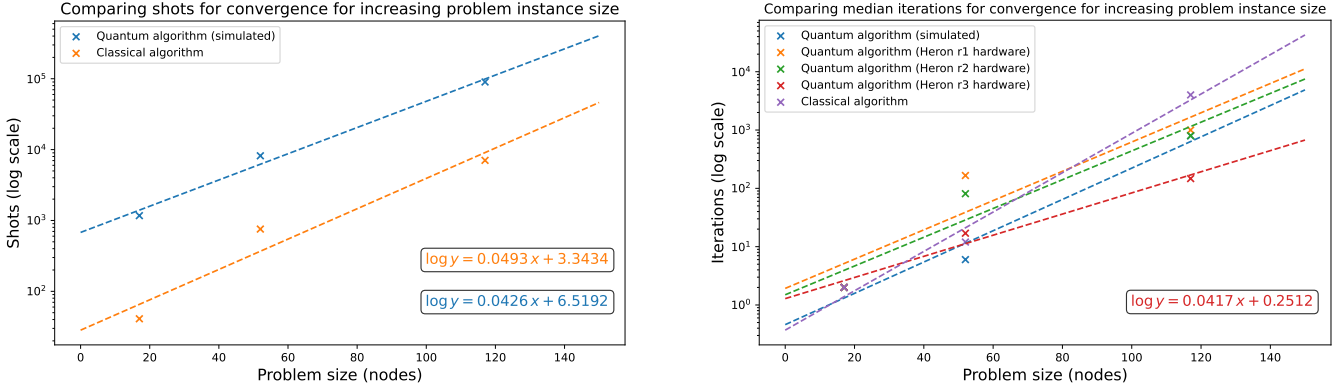


FIG. 4: A summary of anticipated performance scaling in terms of shots and iterations of the classical vs. quantum-enhanced algorithm. Median iterations to converge are reported for the 17, 52 and 117 node graphs after ten repeated tests of the classical and quantum-enhanced algorithms. A line of best fit provides us with a naïve indication of scaling behavior as to how we anticipate each method to perform with increasing problem instance size.

On the left, we present anticipated performance scaling in terms of shots for the classical vs. simulated quantum-enhanced algorithm, using the *Qiskit Aer* MPS simulator. On the right, we see anticipated performance scaling in terms of iterations of the classical vs. quantum-enhanced algorithm, both simulated and run on real hardware.

Three generations of the IBM quantum *Heron* devices were tested for each of the problem instances here, specifically *Heron r1* (`ibm_torino`), *Heron r2* (`ibm_aachen`) and *Heron r3* (`ibm_boston`), where *Heron r3* devices have the lowest error rates of the IBM Quantum superconducting fleet at the time of writing. The relevant data for each device is available via the IBM Quantum platform.

Generally, the gradients of the fitted lines in the right-hand side plot of Figure 4 are worse than on the left plot. Yet, the gradient of the red line, on the right of Figure 4, representing the *Heron r3* device results, has a slightly improved gradient to those reported on the left. These *Heron r3* hardware results outperform both the equivalent classical MCMC test, and the MPS simulated quantum algorithm. Again, this suggests a promising scaling property for the quantum algorithm with larger problem instances, both in comparison to its predecessor hardware and with regards to both the classical and simulated quantum approaches. Interestingly, for the 52 node problem on the right of Figure 4, the MPS simulation performs best. However, for the 117 node instance, the MPS simulation is outperformed by the real *Heron r3* hardware. At the same time, with reduced hardware noise, the quantum device outperforms the simulation. From the data provided so far, we see evidence of promising scaling behavior of our quantum-enhanced algorithm with respect to problem size. With larger and improved quantum hardware, we intend to collect data for larger problem instances to understand which approach continues to show better scaling behavior, since we acknowledge only three non-trivial problem instances were studied in this manuscript. More data is required to draw stronger conclusions.

V. DISCUSSION & CONCLUSIONS

As quantum computing hardware continues to improve, the reliable execution of quantum optimization experiments for non-trivial systems comes within reach. More explicitly, we can execute experiments that study larger and harder problems, and provide an example pathway for seeking quantum advantage in optimization. This is well-supported by benchmarking which enables the community to explore the strengths of classical and quantum algorithms in solving combinatorial optimization problems. Open-source quantum optimization benchmarking frameworks like QOBLIB, from which the majority of problem instances studied here are sourced, help us to understand how we move from utility scale quantum experiments towards advantage in optimization.

In this manuscript, we explore a quantum solver based on a QeMCMC sampling routine to solve non-trivial combinatorial optimization problem instances. We have adapted the QeMCMC workflow to incorporate a warm-started optimization procedure and intentional bias to our proposal distribution towards “good” solutions. We also combine a parallel tempering approach to explore the available cost landscape more efficiently, which is regularly used to find ground states of many-body systems. This heuristic quantum-classical algorithm has been tested against problem instances with up to 117 decision variables, corresponding to 117 qubits on real quantum hardware. While our method does not have provable convergence guarantees, we recover the global optimum for problem instances with 17, 52, and 117 variables.

The results presented indicate early evidence of a scaling advantage compared to classical MCMC approaches for the chosen problem instances. Interestingly, we also see the quantum hardware outperform MPS simulations for the considered setting. We intend to explore larger problem instances to improve our understanding of the scaling of these methods beyond current hardware size limitations.

While encouraging heuristic approaches such as the quantum-classical sampling algorithm described here continue to be developed across the optimization community, we can see there is much optimism to be found in anticipating utility, and even advantage, before fault tolerance in quantum optimization.

Note added regarding concurrent work

During the final preparation of this manuscript, a closely related preprint appeared that proposes a similar overall idea including small-scale classical simulation [53]. Our contribution differs in that we demonstrate the method experimentally on quantum hardware using over 100 qubits. We also introduce practical details and evaluate the concrete circuit designs and implementation-level improvements required to achieve scalable execution.

ACKNOWLEDGMENTS

Acknowledgements - The authors thank David Layden, Mario Motta, Lewis W. Anderson, Benjamin Jaderberg, Lev S. Bishop, Stephan Eidenbenz, Reuben Tate, Antonio Mezzacapo, Max Rossmannek, Stefano Mensa and Jason Crain for helpful discussions and insight.

This work was supported by the Hartree National Centre for Digital Innovation, a collaboration between the Science and Technology Facilities Council and IBM.

Appendix A: Boltzmann sampling

In the present manuscript, we implement circuits that resemble a first-order Trotter approximation of the discretized annealing Hamiltonian presented in Eq. (10). This is as opposed to the second-order Trotter formulation used for circuits constructed in Ref. [15]. Using the first-order approximation is possible since we are not so concerned with Trotter error in the scope of this work. Additionally, the first-order Trotter approximation resembles QAOA, which is useful in our setup when scaling to > 100 variable system sizes, as we can leverage advanced QAOA tools for optimizing parameters at these scales, such as MPS-based energy evaluators for classically tuning γ and β parameters. We demonstrate that with circuits resembling Eq. (19), our first-order Trotter decomposition of QeMCMC is still effective for sampling.

In preparation for using QeMCMC in the heuristic setting implemented in this paper, we conduct small-scale Boltzmann sampling experiments for various temperatures, as were performed in Ref. [15]. We do this using a small, five-node MIS problem instance. Owing to the modest dimensionality of this system, the complete distribution over computational basis states can be readily visualized. In Figure 5, we see the theoretical Boltzmann distribution for this problem instance. Here, the Ising-like energies are computed by enumerating all 2^n bit-strings $\{s_i\}$ and evaluating their energies $E_i = E(s_i)$ under the MIS Hamiltonian. The corresponding probabilities are then obtained from the Boltzmann distribution defined in Eq. (1), yielding the exact classical distribution at temperature T . In Figure 6a, we demonstrate the iterative process of converging to the desired Boltzmann distributions at $T = 0.1$, where $k_B = 1$ on IBM Quantum superconducting hardware. When Ref. [15] was originally published, the authors were limited from running these experiments end-to-end, within one execution window. This was due to limitations of running iterative experiments on the available quantum hardware, which is explained fully in the associated work [15]. However, this execution style is now well-supported with **Qiskit Runtime** Session mode. In the work presented here, we use Session mode alongside parameter streaming capabilities, which provide a tight classical feedback loop for determining circuit parameters based on quantum experimental results, within the Session window. The results shown in Figure 6a and Figure 6b were obtained in this way, which allows for efficient job batching and reduced queuing latency.

These results are produced by first formulating the MIS problem for the five node problem using a Hamiltonian defined by the graph, to produce QAOA circuits of the form in Eq. (19), and then proceeding as per the logic described in Section III A. The QAOA circuits are used to construct a proposal, Q , explained in Section III F. We build Q in the form of a dense matrix where each column is updated according to the starting state, s , and sampled solutions, s' , drawn from the quantum circuit. For a small problem like this, we can extract all components of this matrix exactly using brute force to build the full statevector, then enumerate until we have the full analytical matrix for Q . For larger problems, we would need to sample from quantum circuits to build up this matrix progressively, since the approach described here is resource intensive. We can also utilize sparse matrix approaches to approximate the matrix. Via both methods, we derive empirical probabilities of possible end states, s' , from the start state, s .

Next, we apply the MH acceptance probability as defined in Eq. (4), to construct a transition matrix, P , from the proposal matrix, Q , equivalent to P in Eq. (3). The resulting transition matrix is stochastic, and fully describes our Markov chain, incorporating both the proposal distribution and the MH acceptance rule.

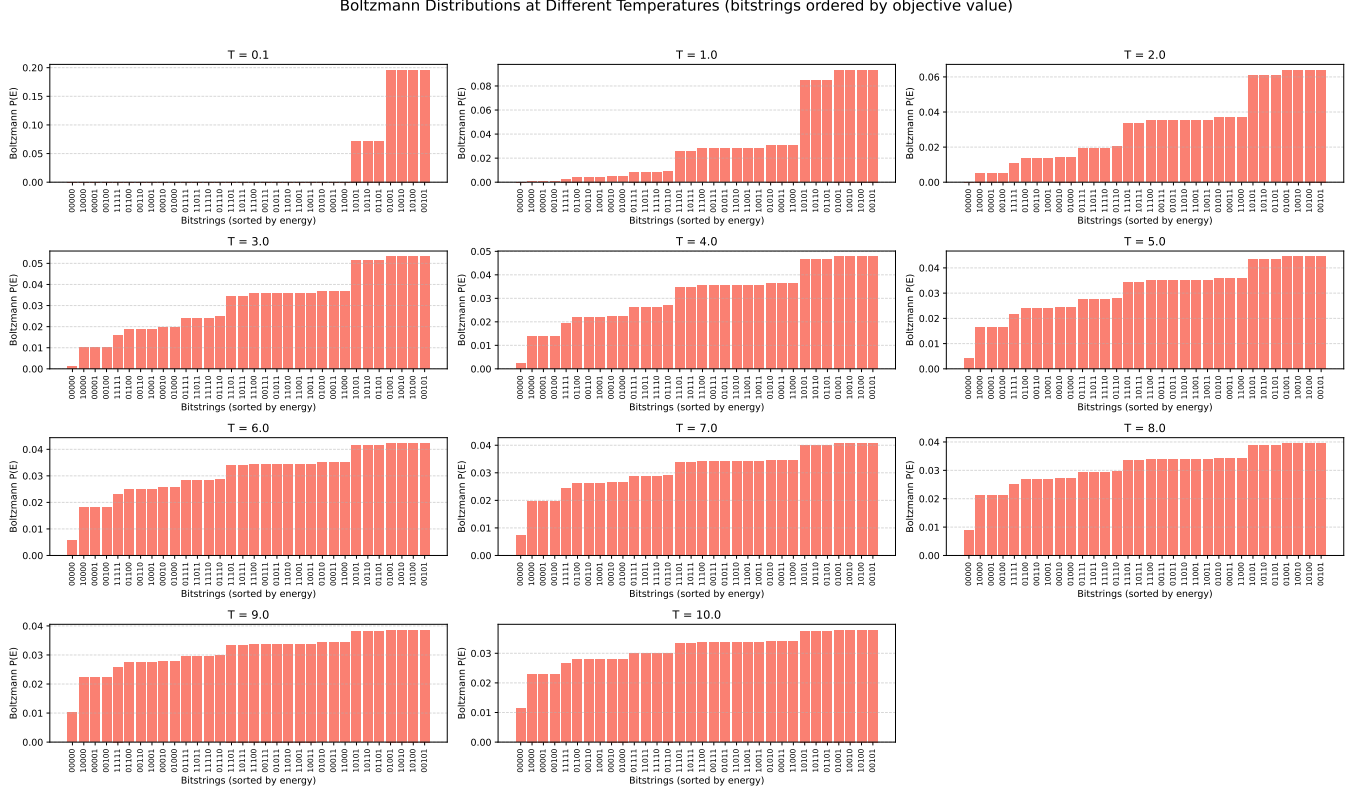


FIG. 5: Theoretical distribution for a five node MIS problem instance, for a range of (dimensionless) temperatures T .

Our transition matrix, P , is then used to generate moves in the Markov chain, and over many iterations, or steps, we can construct plots like that shown in Figure 6a and in Figure 6b. From this, we can check that our stationary distribution is an eigenstate of the transition matrix, Q .

We note that there is a general assumption within the community that high-performance computing (HPC) resources are required for implementing QeMCMC at non-trivial scales. In our work, HPC resources were used for a number of tasks both in experiment preparation and post-processing results, such as with parameter optimization and classical simulation experiments of the larger quantum circuits used herein. However, generally, we avoided excessive use of HPC resources during the algorithm execution window by pre-emptively compiling circuits and using known QAOA best practices to scale our experiments. We also acknowledge that QeMCMC algorithms generally rely on a fast exchange of information between sampling from the quantum computer and a classical evaluation procedure to accept or reject a proposal. For the scales of problems investigated here, up to 117 qubits, the use of remote APIs, such as the **Qiskit Runtime** Session mode mentioned previously, were sufficient for our use case. However, we anticipate the classical computational demand of this algorithm to increase as we look to solve larger problem instances.

Appendix B: Maximum independent set mapping

We briefly explain the mapping from the QUBO defined in Eq. (8), to a Hamiltonian of the form

$$H_{\text{cost}} = H_{\text{objective}} + \lambda H_{\text{constraint}},$$

up to a constant energy shift. We use a mapping with the relevant Paulis $x_i = (1 - Z_i)/2$, such that the MIS objective can be written as

$$\sum_i x_i = \frac{|V|}{2} - \frac{1}{2} \sum_i Z_i = \frac{|V|}{2} + H_{\text{objective}}, \quad (B1)$$

where $H_{\text{objective}} = -\frac{1}{2} \sum_i Z_i$, up to an additive constant.

Similarly, the constraint penalty becomes

$$\begin{aligned} -\lambda \sum_{(v_i, v_j) \in E} x_i x_j &= -\frac{\lambda}{4} \sum_{(v_i, v_j) \in E} (1 - Z_i - Z_j + Z_i Z_j) \\ &= -\frac{\lambda |E|}{4} + \lambda H_{\text{constraint}}, \end{aligned} \quad (B2)$$

where

$$H_{\text{constraint}} = \frac{1}{4} \sum_{(v_i, v_j) \in E} (Z_i Z_j - Z_i - Z_j),$$

again up to an additive constant.

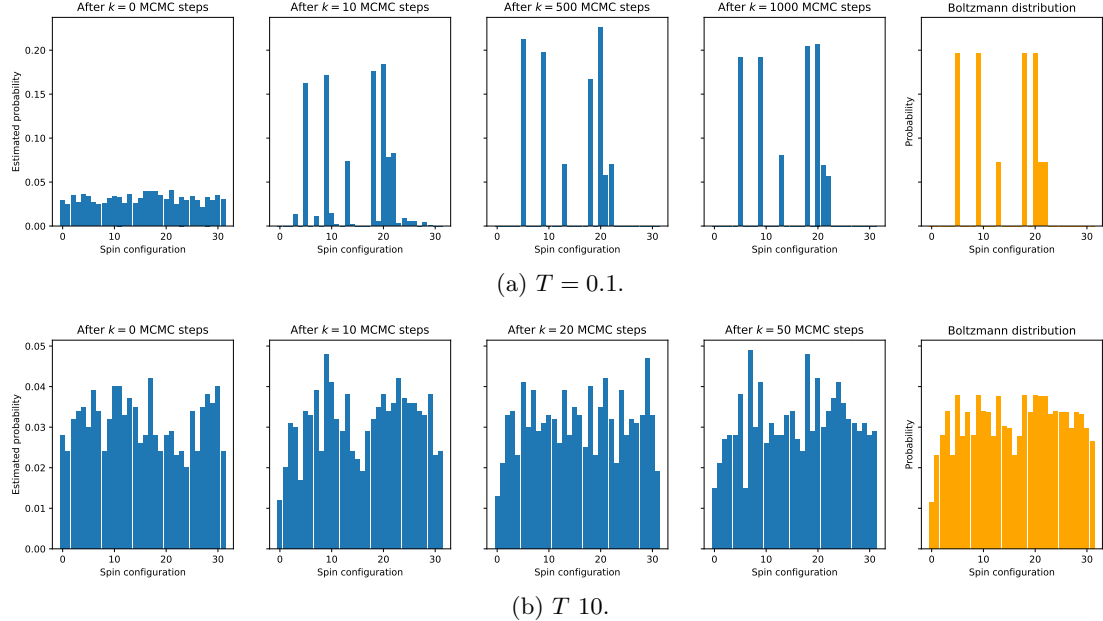


FIG. 6: Convergence to the stationary distribution for QeMCMC experiment at a high and low temperature.

Here, the first term is a constant energy offset, while the remaining terms define the Hamiltonian encoding the constraints of the maximum independent set problem. These terms consist of single-qubit contributions proportional to Z_i and pairwise interaction terms of the form $Z_i Z_j$. Upon promoting the classical spin variables to Pauli-Z operators, the independent set objective and constraints take the form of a classical Ising Hamiltonian,

$$H_{\text{Ising}} = - \sum_i h_i Z_i - \sum_{(v_i, v_j) \in E} J_{ij} Z_i Z_j, \quad (\text{B3})$$

where the coefficients h_i and J_{ij} arise directly from the linear and quadratic operator terms in Eqs. (B1) and (B2), up to a similar additive constant.

Finally, while the MIS problem is naturally posed as a maximization of the objective $\sum_i x_i$, we adopt the standard physics convention of defining an energy function as the negative of this objective (with additional penalty terms), thereby converting the problem into an equivalent energy minimization task whose ground states correspond to optimal solutions.

Appendix C: Circuit optimization

In this Section, we discuss the tuning of parameters for individual QeMCMC replica circuits, which resemble $p = 2$ QAOA. The MIS problem is mapped to a QUBO, described by an Ising Hamiltonian H_{cost} , by adding the constraints as penalty terms. The optimization landscape of our encoded problem changes with the value of this penalty term. As such, we tune this term in

such a way that smoothens this landscape, generally with smaller penalty values. The state $\psi(\beta, \gamma; \lambda)$ constructed on the hardware thus depends on the QAOA angles (β, γ) and the Lagrange multiplier λ . The latter is set by an optimization procedure that tries to equate the expectation value of the objective terms in $H_{\text{objective}}$ and the constraint terms of $H_{\text{constraint}}$ when sampling from $|\psi\rangle$, see details in Ref. [13]. This can result in good quality samples s drawn from $|\psi\rangle$ when executed on quantum hardware, even though the ground state of H_{cost} is not necessarily the same as the solution of the MIS problem when $\lambda < 2$.

For each explored value of λ , the QAOA angles are optimized classically with the *QAOA Training Pipeline* [46]. This open-source package allows one to design a chain of parameter trainers to find β and γ in $|\psi\rangle$ along with the methods to evaluate the energy $\langle \psi | H_{\text{cost}} | \psi \rangle$. To train parameters for our $p = 2$ QAOA we first find optimal depth $p = 1$ parameters with `SciPy` running COBYLA from the initial point $\beta_1 = 0$ and $\gamma_1 = 0$. Next, the resulting optimal β_1^* and γ_1^* are used as the initial point for a transition state trainer to find the parameters at depth $p = 2$. A constraint is applied such that $\gamma_1 = \gamma_2 \equiv \gamma$ and $\beta_1 = \beta_2 \equiv \beta$, as is discussed at the beginning of Section III F. Here, since we use $p = 2$ QAOA, three transition states are explored and the QAOA angles with the best energy are used [54]. The energy is evaluated approximately with an MPS operating at various thresholds of 10^{-6} to 10^{-10} , largely to ensure energies have converged with respect to truncation threshold.

Finally, to further enable our QAOA circuits which are used to generate the proposal distribution in our

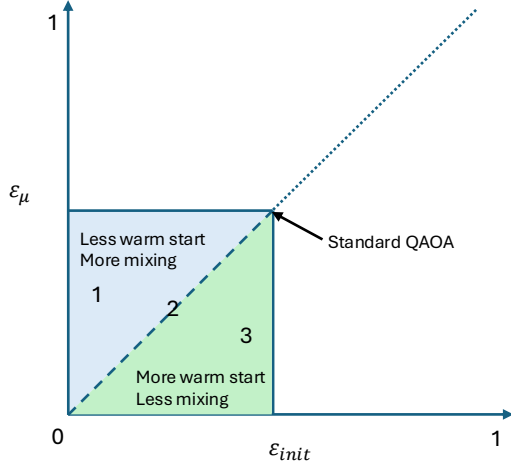


FIG. 7: Visualization of different combinations of parameters $\varepsilon_{\text{init}}$ and ε_{μ} . Regions labeled 1, 3 and 2, which indicate more or less warm starting and mixing respectively, were all tested in this work.

quantum-enhanced solver, we bias our circuits with a warm-starting implementation, as discussed in Section III B. First, a relaxed version of the original problem is solved with a quantum circuit, and the resulting solution is used to warm-start the next iteration of our algorithm. This process is visualized in Figure 1. To do this, we extend the work documented in Ref. [26].

The process involves defining a regularization parameter, ε , which determines the rotation angles used in the initial state and mixer layer of subsequent QAOA circuits, as described in Section III B. In this work, when tuning ε , we began testing with the same values originally used by authors in Ref. [26]. We also scanned nearby values to this starting point and tested for optimal performance. Finally, we also tried explicitly separating ε for defining the $R_y(\theta)$ rotations applied to the initial state, $\varepsilon_{\text{init}}$, and for the mixer, ε_{μ} , such that we could explore the continuum of options between partially and fully warm starting our circuits, or not at all. The different regimes we explored in the work documented in this paper are visualized in Figure 7. However, we observed that the area of alignment between $\varepsilon_{\text{init}}$ and ε_{μ} , i.e. on the diagonal of the plot, leads to the most performant results. This result agrees with conclusions made in Ref. [55]. With an aligned mixer constructed such that $|s_\theta\rangle$ is its ground state, we can also expect to preserve the convergence guarantee in the limit $p \rightarrow \infty$ [28].

Appendix D: Tuning the parallel tempering experimental setup

In this Appendix, we explain how the parameters used in the parallel tempering setup were selected. As a re-

minder, parallel tempering was initially developed to improve MCMC sampling of Gibbs distributions [34–36], but it is also commonly adapted as an optimization tool to find low-energy or ground-state solutions, where we expect the target ground state energy to coincide with the expected value of the Gibbs free energy of a low temperature replica of the parallel tempering experiment [37, 56]. Accordingly, we use several standard design considerations from the parallel tempering literature [34–38, 48, 49, 57, 58] to guide our experiments.

Firstly, determining the number of replicas and their corresponding temperatures is key in ensuring algorithmic performance [37]. In parallel tempering, the maximum temperature T_{high} should be chosen so that replicas can escape local energy minima, while the number of replicas must be sufficient to allow swaps to occur reliably between adjacent temperature levels. In our setup, we determined the temperature range by first computing the maximum temperature using an inverted Boltzmann factor,

$$T_{\text{high}} = \left| -\frac{x_{\text{max}}}{k_B \ln P_{\text{high}}} \right|, \quad (\text{D1})$$

where x_{max} is the largest eigenvalue of H_{cost} , which is pre-computed for our smaller problem instance of 17 qubits using exact diagonalization. Since studying the spectrum of the Hamiltonian in this way is only possible for our smallest problems, we must rely on the fact that our problem instances are closely related in exhibiting heterogeneous degree distributions and nontrivial interaction structure. As such, we can appropriately extrapolate these values for the larger related problem instances as a starting point, before tuning these values experimentally. P_{high} is the target acceptance probability for high temperature moves, in our examples we choose a sensible value guided by the literature $P_{\text{high}} \geq 0.5$. The minimum temperature should be a small-fixed value to allow adequate sampling of low-energy states. We further tune temperatures experimentally to gauge a setting that leverages optimal performance on the hardware. Based on heuristic MCMC test runs, we clip $T_{\text{low}} = 0.01$, i.e. to just above zero, in our experiments. This is necessary to ensure that there is always a non-zero probability of a transition even in cases where proposed moves result in higher energy solutions.

With the temperature range fixed, the number of replicas N was similarly chosen heuristically to achieve adequate swap acceptance between adjacent temperatures. For a fixed range $[T_{\text{low}}, T_{\text{high}}]$, we increased the number of replicas until adjacent temperatures yield satisfactory swap acceptance probabilities, typically in the range 20-40% [48, 57]. We then constructed a geometric temperature ladder

$$T_i = T_{\text{low}} \left(\frac{T_{\text{high}}}{T_{\text{low}}} \right)^{\frac{i-1}{N-1}}, \quad (\text{D2})$$

for $i = 1, 2, \dots, N$.

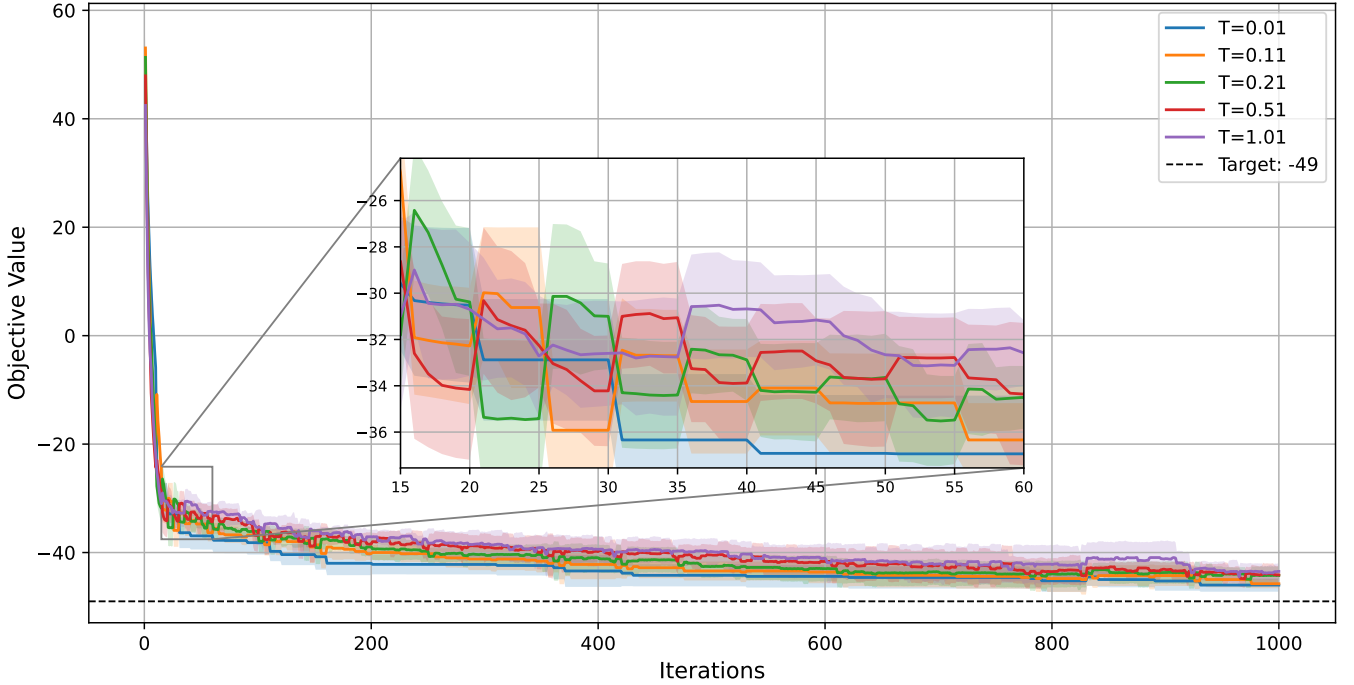


FIG. 8: 117 node graph MIS problem results, using an MPS-based sampling simulation of the quantum circuits. Iterations of the algorithm are plotted against the computed objective values, or energy, at each iteration. Each iteration involves taking 10,000 samples, and randomly subsampling from a smaller subset of these samples. The results plotted are mean values with error bars computed from standard deviations, using ten repeats of the simulated tests. The inset shows faster mixing of individual replicas via replica exchange at regular intervals, towards the converged solution with an energy of -49 .

This spacing concentrates replicas at lower temperatures (where energy barriers are more pronounced) while still permitting replicas with higher temperatures [49].

Next, we consider the replica-exchange regularity, defined by the parameter $\Delta t_{\text{swap}} = 1/k$. Let k denote the number of local MCMC updates performed between consecutive exchange attempts (so an exchange is attempted after every k local updates). We selected k experimentally to yield satisfactory swap acceptance probabilities. In our setup, k was chosen in the range $1 \leq k \leq 5$. Furthermore, in the replica exchange stage of the algorithm, there exist several ways to implement the exchange step [58]. In this work, we used a stochastic even-odd algorithm. Let $\mathcal{N} = \{(i, i+1) \mid i = 1, \dots, N-1\}$ be the set of neighboring replica pairs in the temperature ladder. Furthermore, define the even and odd subsets: $\mathcal{E} = \{(2j, 2j+1)\}$, $\mathcal{O} = \{(2j-1, 2j)\}$. At each iteration, we alternate between even and odd replica pairs, and swap attempts are performed for all pairs within the selected subset. This allows exchanges that propagate information down the temperature ladder toward the coldest chains. The algorithm then proceeds until termination, which in our setup occurs either when a target objective value is reached or when 200,000 iterations are exhausted.

An example MPS simulation of the parallel tempering experiment run on hardware in Figure 2 is presented in Figure 8, where the zoomed in panel allows us to visualize the replica exchange process at work.

Appendix E: QAOA ansatz construction

QAOA composes an ansatz circuit following Eq. (19). Of course, the graph topologies of the problem instances used do not match the qubit connectivity graphs of the quantum hardware. Therefore, implementing the full cost operator requires deep networks of SWAP gates, even when advanced compilation and transpilation tools are employed, which themselves introduce various SAT mappings and SWAP strategies to try to reduce circuit depth [46]. For example, the 117 node problem would require a two-qubit gate depth of 696 to fully implement $e^{-i\gamma H_{\text{cost}}}$. These deep circuits are problematic for noisy quantum hardware. Indeed, beyond a certain circuit depth, the gains of capturing more of the structure of the problem through additional SWAP gates is eroded by device noise. This tradeoff was explored in Ref. [59] on random 3-regular graphs, where best samples were obtained by a $p = 2$ QAOA. This simplified ansatz H_{cost} was chosen by allowing 2 or 3 layers of SWAP gates.

We construct simplifications of the problem that we can execute, by applying a SWAP network to the graph [59, 60]. The simplest instances are effectively hardware native graphs. We generate subgraphs of the problem that are overlapping, and become incrementally more complex (in terms of density of edges in the graph) with more SWAP layers allowed, resulting in a higher overlap with the full graph. From these subgraphs, we can select an ansatz circuit that sensibly balances quality of samples with feasibility to run on hardware. The QAOA ansatz that we implement is given by

$$U_{\text{QAOA}} = e^{-i\beta_2 H_{\text{mix}}} e^{-i\gamma_2 H'_{\text{cost}}} e^{-i\beta_1 H_{\text{mix}}} e^{-i\beta_2 H'_{\text{cost}}} \quad (\text{E1})$$

where H'_{cost} implements only the subset of the $Z_i Z_j$ terms that can be implemented with two layers of SWAP gates on a line of qubits.

In choosing the ansatz for each of the problem instances, we study the behavior seen when increasing the number of SWAP layers to see whether this also increases the quality of the samples. We tune the quality of the QAOA circuit ansatz, to understand where sample quality no longer increase with the number of SWAP layers allowed, and after what point we see noise degrading the results. We observe how the quality of the ansatz performs for a $p = 2$ QAOA given a maximum number of SWAP layers, k . We optimize angles for the QAOA for the chosen (p, k) as per the process described in Appendix C. Finally, we draw samples from the hardware and compute the average approximation ratio of the resulting objectives, for each of four possible ansaetze to be studied, in this example for the 52 node graph problem. Since we are working with constrained optimization, we filter for valid samples before computing their objective values and taking an average for the approximation ratio. We also test with and without a classical correction step for the proposed

solutions to the MIS. This is a classical post-processing step that aggressively removes nodes across the proposals that violate the constraints for the MIS problem. The solution is then improved upon where possible. We apply this classical correction step in this analysis, since the full iterative algorithm proposed in this paper is not used and we are only testing the quality of samples from the ansaetze. It is noted that even classically corrected samples from the ansaetze circuits tested without the iterative algorithm approach presented in this paper are not able to reach the true solution to this 52 node problem.

Using the results in Table IV, we see how number of SWAP layers, k , affects quality of the ansaetze, informing our choice of ansatz for our algorithm. When we consider only feasible solutions to the raw circuit samples, we see quality of the samples (measured by the value of the approximation ratio between $[0, 1]$) steadily increase up to 37 SWAP layers, and then degrade. For those solutions that have been classically corrected, the approximation ratios are higher. The 37 and 49 SWAP layer ansaetze are most successful, since they have the highest overlap with the full graph. With this, we justify our decision to use the 37 SWAP layer ansatz for this 52 node problem.

Nodes/qubits	No. SWAP layers	Classical post-processing	Approx. ratio
52	13	False	0.0172
52	25	False	0.0241
52	37	False	0.0403
52	49	False	0.0394
52	13	True	0.9074
52	25	True	0.9002
52	37	True	0.9109
52	49	True	0.9111

TABLE IV: Approximation ratios taken for various ansaetze to the full 52 node graph, given a number of allowed SWAP layers.

[1] A. Abbas, A. Ambainis, B. Augustino, A. Bärtschi, H. Buhrman, C. Coffrin, G. Cortiana, V. Dunjko, D. J. Egger, B. G. Elmegreen, N. Franco, F. Fratini, B. Fuller, J. Gacon, C. Gonciulea, S. Gribling, S. Gupta, S. Hadfield, R. Heese, G. Kircher, T. Kleinert, T. Koch, G. Korpas, S. Lenk, J. Marecek, V. Markov, G. Mazzola, S. Mensa, N. Mohseni, G. Nannicini, C. O’Meara, E. P. Tapia, S. Pokutta, M. Proissl, P. Rebentrost, E. Sahin, B. C. B. Symons, S. Tornow, V. Valls, S. Woerner, M. L. Wolf-Bauwens, J. Yard, S. Yarkoni, D. Zechiel, S. Zhuk, and C. Zoufal, Challenges and opportunities in quantum optimization, *Nature Reviews Physics* **6**, 718–735 (2024).

[2] E. Farhi, J. Goldstone, S. Gutmann, J. Lapan, A. Lundgren, and D. Preda, A quantum adiabatic evolution algorithm applied to random instances of an np-complete problem, *Science* **292**, 472–475 (2001).

[3] E. Farhi, J. Goldstone, and S. Gutmann, A quantum approximate optimization algorithm applied to a bounded occurrence constraint problem (2015), arXiv:1412.6062 [quant-ph].

[4] M. B. Hastings, A short path quantum algorithm for exact optimization (2018), arXiv:1802.10124 [quant-ph].

[5] J. Basso, E. Farhi, K. Marwaha, B. Villalonga, and L. Zhou, The quantum approximate optimization algorithm at high depth for maxcut on large-girth regular graphs and the sherrington–kirkpatrick model, in *Proceedings of the 17th Conference on the Theory of Quantum Computation, Communication and Cryptography (TQC 2022)*, Vol. 232 (Schloss Dagstuhl – Leibniz-Zentrum für Informatik, 2022) pp. 7:1–7:21.

[6] A. M. Dalzell, N. Pancotti, E. T. Campbell, and F. G. Brandão, Mind the gap: Achieving a super-grover quantum speedup by jumping to the end, in *Proceedings of the 55th Annual ACM Symposium on Theory of Computing*, STOC ’23 (ACM, 2023) p. 1131–1144.

[7] R. Shaydulin, C. Li, S. Chakrabarti, M. DeCross, D. Herman, N. Kumar, J. Larson, D. Lykov, P. Minssen, Y. Sun, Y. Alexeev, J. M. Dreiling, J. P. Gaebler, T. M. Gatter-

man, J. A. Gerber, K. Gilmore, D. Gresh, N. Hewitt, C. V. Horst, S. Hu, J. Johansen, M. Matheny, T. Menngle, M. Mills, S. A. Moses, B. Neyenhuis, P. Siegfried, R. Yalovetzky, and M. Pistoia, Evidence of scaling advantage for the quantum approximate optimization algorithm on a classically intractable problem, *Science Advances* **10**, 10.1126/sciadv.adm6761 (2024).

[8] E. Farhi, J. Goldstone, and S. Gutmann, A quantum approximate optimization algorithm (2014), arXiv:1411.4028 [quant-ph].

[9] J. Wurtz and P. Love, Maxcut quantum approximate optimization algorithm performance guarantees for $p \geq 1$, *Physical Review A* **103**, 10.1103/physreva.103.042612 (2021).

[10] P. Chandarana, A. G. Cadavid, S. V. Romero, A. Simen, E. Solano, and N. N. Hegade, Runtime quantum advantage with digital quantum optimization (2025), arXiv:2505.08663 [quant-ph].

[11] J. Eisert and J. Preskill, Mind the gaps: The fraught road to quantum advantage (2025), arXiv:2510.19928 [quant-ph].

[12] Y. Kim, A. Eddins, S. Anand, *et al.*, Evidence for the utility of quantum computing before fault tolerance, *Nature* **618**, 500 (2023).

[13] T. Koch, D. E. B. Neira, Y. Chen, G. Cortiana, D. J. Egger, R. Heese, N. N. Hegade, A. G. Cadavid, R. Huang, T. Itoko, T. Kleinert, P. M. Xavier, N. Mohseni, J. A. Montanez-Barrera, K. Nakano, G. Nannicini, C. O'Meara, J. Pauckert, M. Proissl, A. Ramesh, M. Schicker, N. Shimada, M. Takeori, V. Valls, D. V. Bulck, S. Woerner, and C. Zoufal, Quantum optimization benchmarking library - the intractable decathlon (2025), arXiv:2504.03832 [quant-ph].

[14] G. Mazzola, Sampling, rates, and reaction currents through reverse stochastic quantization on quantum computers, *Phys. Rev. A* **104**, 022431 (2021).

[15] D. Layden, G. Mazzola, R. V. Mishmash, M. Motta, P. Wocjan, J.-S. Kim, and S. Sheldon, Quantum-enhanced markov chain monte carlo, *Nature* **619**, 282–287 (2023).

[16] A. Orfi and D. Sels, Barriers to efficient mixing of quantum-enhanced markov chains, *Physical Review A* **110**, 052434 (2024).

[17] A. Orfi and D. Sels, Bounding the speedup of the quantum-enhanced markov-chain monte carlo algorithm, *Physical Review A* **110**, 052414 (2024).

[18] S. Ferguson and P. Wallden, Quantum-enhanced markov chain monte carlo for systems larger than a quantum computer, *Physical Review Research* **7**, 013231 (2025).

[19] J. Christmann, P. Ivashkov, M. Chiurco, and G. Mazzola, From quantum-enhanced to quantum-inspired monte carlo, *Physical Review A* **111**, 042615 (2025).

[20] L. Chang, Z. Li, and W.-H. Fang, Quantum-assisted variational monte carlo, *Precision Chemistry* (2025).

[21] S. Bravyi, O. Dial, J. M. Gambetta, D. Gil, and Z. Nazario, The future of quantum computing with superconducting qubits, *Journal of Applied Physics* **132**, 10.1063/5.0082975 (2022).

[22] S. Geman and D. Geman, Stochastic relaxation, gibbs distributions, and the bayesian restoration of images, *IEEE Transactions on Pattern Analysis and Machine Intelligence* **PAMI-6**, 721 (1984).

[23] N. Metropolis, A. W. Rosenbluth, M. N. Rosenbluth, A. H. Teller, and E. Teller, Equation of state calculations by fast computing machines, *The Journal of Chemical Physics* **21**, 1087 (1953).

[24] W. K. Hastings, Monte carlo sampling methods using markov chains and their applications, *Biometrika* **57**, 97 (1970).

[25] M. Mezard and A. Montanari, *Information, Physics, and Computation* (Oxford University Press, Inc., USA, 2009).

[26] D. J. Egger, J. Mareček, and S. Woerner, Warm-starting quantum optimization, *Quantum* **5**, 479 (2021).

[27] R. Tate, M. Farhadi, C. Herold, G. Mohler, and S. Gupta, Bridging classical and quantum with sdp initialized warm-starts for qaoa (2022), arXiv:2010.14021 [quant-ph].

[28] R. Tate, J. Moondra, B. Gard, G. Mohler, and S. Gupta, Warm-started qaoa with custom mixers provably converges and computationally beats goemans–williamson’s max-cut at low circuit depths, *Quantum* **7**, 1121 (2023).

[29] M. Cain, E. Farhi, S. Gutmann, D. Ranard, and E. Tang, The qaoa gets stuck starting from a good classical string (2023), arXiv:2207.05089 [quant-ph].

[30] S. Feeney, R. Tate, and S. Eidenbenz, The better solution probability metric: Optimizing qaoa to outperform its warm-start solution (2024), arXiv:2409.09012 [quant-ph].

[31] R. Tate and S. Eidenbenz, Theoretical approximation ratios for warm-started qaoa on 3-regular max-cut instances at depth $p = 1$ (2024), arXiv:2402.12631 [quant-ph].

[32] R. Tate and S. Eidenbenz, Warm-started qaoa with aligned mixers converges slowly near the poles of the bloch sphere (2024), arXiv:2410.00027 [quant-ph].

[33] B. Bhattacharyya, M. Capriotti, and R. Tate, Solving general qubos with warm-start qaoa via a reduction to max-cut (2025), arXiv:2504.06253 [quant-ph].

[34] R. H. Swendsen and J.-S. Wang, Replica monte carlo simulation of spin-glasses, *Physical review letters* **57**, 2607 (1986).

[35] C. J. Geyer, Markov chain monte carlo maximum likelihood, in *Computing Science and Statistics: Proceedings of the 23rd Symposium on the Interface* (American Statistical Association, New York, 1991) p. 156.

[36] K. Hukushima and K. Nemoto, Exchange monte carlo method and application to spin glass simulations, *Journal of the Physical Society of Japan* **65**, 1604 (1996).

[37] D. J. Earl and M. W. Deem, Parallel tempering: Theory, applications, and new perspectives, *Physical Chemistry Chemical Physics* **7**, 3910 (2005).

[38] S. Brooks, A. Gelman, G. Jones, and X.-L. Meng, *Handbook of markov chain monte carlo* (CRC press, 2011).

[39] K. Temme, S. Bravyi, and J. M. Gambetta, Error mitigation for short-depth quantum circuits, *Physical Review Letters* **119**, 10.1103/physrevlett.119.180509 (2017).

[40] S. Endo, S. C. Benjamin, and Y. Li, Practical quantum error mitigation for near-future applications, *Physical Review X* **8**, 10.1103/physrevx.8.031027 (2018).

[41] A. Kandala, K. Temme, A. D. Córcoles, A. Mezzacapo, J. M. Chow, and J. M. Gambetta, Error mitigation extends the computational reach of a noisy quantum processor, *Nature* **567**, 491–495 (2019).

[42] S. Endo, Z. Cai, S. C. Benjamin, and X. Yuan, Hybrid quantum-classical algorithms and quantum error mitigation, *Journal of the Physical Society of Japan* **90**, 032001 (2021).

[43] S. V. Barron, D. J. Egger, E. Pelofske, A. Bärtschi, S. Eidenbenz, M. Lehmkuehler, and S. Woerner, Provably

bounds for noise-free expectation values computed from noisy samples, *Nature Computational Science* **4**, 865–875 (2024).

[44] P. K. Barkoutsos, G. Nannicini, A. Robert, I. Tavernelli, and S. Woerner, Improving Variational Quantum Optimization using CVaR, *Quantum* **4**, 256 (2020).

[45] D. C. McKay, I. Hincks, E. J. Pritchett, M. Carroll, L. C. G. Goria, and S. T. Merkel, Benchmarking quantum processor performance at scale (2023), arXiv:2311.05933 [quant-ph].

[46] Q. Community, Qaoa training pipeline, https://github.com/qiskit-community/qaoa_training_pipeline (2025).

[47] D. J. Egger, Independent set benchmarking, https://github.com/eggerdj/independent_set_benchmarking (2025).

[48] A. Kone and D. A. Kofke, Selection of temperature intervals for parallel-tempering simulations, *The Journal of chemical physics* **122** (2005).

[49] W. Nadler and U. H. Hansmann, Optimized explicit-solvent replica exchange molecular dynamics from scratch, *The Journal of Physical Chemistry B* **112**, 10386 (2008).

[50] J. D. Chodera and M. R. Shirts, Replica exchange and expanded ensemble simulations as gibbs sampling: Simple improvements for enhanced mixing, *The Journal of chemical physics* **135** (2011).

[51] A. Javadi-Abhari, M. Treinish, K. Krsulich, C. J. Wood, J. Lishman, J. Gacon, S. Martiel, P. D. Nation, L. S. Bishop, A. W. Cross, B. R. Johnson, and J. M. Gambetta, Quantum computing with Qiskit (2024), arXiv:2405.08810 [quant-ph].

[52] IBM, *IBM ILOG CPLEX Optimization Studio*, IBM Corporation (2023).

[53] S. Ferguson and P. Wallden, Methods for non-variational heuristic quantum optimisation (2026), arXiv:2602.01353 [quant-ph].

[54] S. H. Sack, R. A. Medina, R. Kueng, and M. Serbyn, Recursive greedy initialization of the quantum approximate optimization algorithm with guaranteed improvement, *Phys. Rev. A* **107**, 062404 (2023).

[55] Z. He, R. Shaydulin, S. Chakrabarti, D. Herman, C. Li, Y. Sun, and M. Pistoia, Alignment between initial state and mixer improves qaoa performance for constrained optimization, *npj Quantum Information* **9**, 10.1038/s41534-023-00787-5 (2023).

[56] W. Wang, J. Machta, and H. G. Katzgraber, Comparing monte carlo methods for finding ground states of ising spin glasses: Population annealing, simulated annealing, and parallel tempering, *Physical Review E* **92**, 013303 (2015).

[57] U. H. Hansmann, Parallel tempering algorithm for conformational studies of biological molecules, *Chemical Physics Letters* **281**, 140 (1997).

[58] M. Lingenheil, R. Denschlag, G. Mathias, and P. Tavan, Efficiency of exchange schemes in replica exchange, *Chemical Physics Letters* **478**, 80 (2009).

[59] S. Drăgoi, A. Baiardi, and D. J. Egger, Approximate quadratization of high-order hamiltonians for combinatorial quantum optimization (2025), arXiv:2505.04700 [quant-ph].

[60] J. Weidenfeller, L. C. Valor, J. Gacon, C. Tornow, L. Bello, S. Woerner, and D. J. Egger, Scaling of the quantum approximate optimization algorithm on superconducting qubit based hardware, *Quantum* **6**, 870 (2022).